Vol. 32 • No. 28 • July 16 • 2020

www.advmat.de

ADVANCED MATERIALS

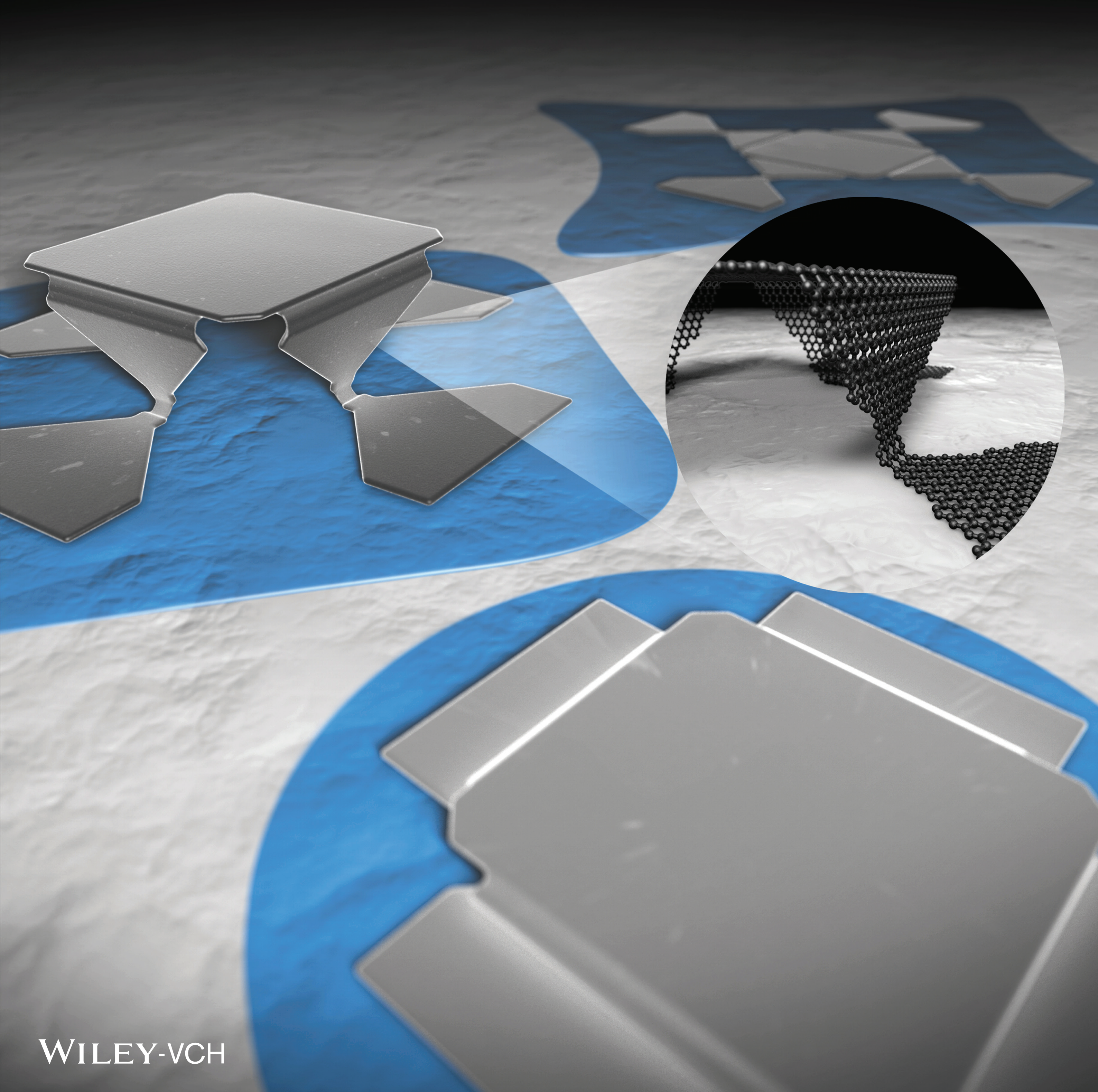

WILEY-VCH

Assembly of Foldable 3D Microstructures Using Graphene Hinges

Seungyun Lim, Haiwen Luan, Shiwei Zhao, Yongjun Lee, Yihui Zhang, Yonggang Huang, John A. Rogers,* and Jong-Hyun Ahn**

Origami/kirigami-inspired 3D assembly approaches have recently attracted attention for a variety of applications, such as advanced optoelectronic devices and biomedical sensors. The results reported here describe an approach to construct classes of multiple foldable 3D microstructures that involve deformations that typical conductive materials, such as conventional metal films, cannot tolerate. Atomically thin graphene sheets serve as folding hinges during a process of 2D to 3D conversion via a deterministic buckling process. The exceptional mechanical properties of graphene enable the controlled, geometric transformation of a 2D precursor bonded at selective sites on a prestretched elastomer into folded 3D microstructures, in a reversible manner without adverse effects on the electrical properties. Experimental and computational investigations of the folding mechanisms for such types of 3D objects reveal the underlying physics and the dependence of the process on the thickness of the graphene/supporting films that define the hinges.

Recently, 3D microstructures have attracted great interest owing to emerging applications in foldable microelectronics,[1–4] piezoelectric microsystems,[5] micro-electromechanical systems,[6–9] wireless electronic devices,[10,11] deformable batteries,[12,13] biosensors,[14,15] and light-tracking photodetectors.[16–19] Fabrication of 3D microstructures by using 2D planar processes based on lithography and printing techniques, commonly utilized in current electronic device manufacturing processes, can be extremely challenging.[7,14,15] To address this issue, numerous methods including surface-tension-based assembly;[20] electric,[21] magnetic,[22] thermal,[23,24] and shape-memory alloy actuation;[25] and residual stress-driven actuation[26–28] have been investigated. Alternatively, Deng et al. reported an approach to create self-folded or rolled 3D structures using graphene and SU8 bilayers responsive to solvent change.[29]

These approaches, however, cannot be applied to many classes of electronic materials including certain metals and semiconductors and/or they have limited ability to achieve 3D geometries in a deterministic manner.[30] As an alternative, controlled processes of mechanical 3D assembly using methods inspired by origami/kirigami are of interest because of their practicality and compatibility with established 2D fabrication methods.[31–35] A specific approach of this general class converts 2D precursor structures bonded at selected sites to the prestretched elastomer substrates into desired 3D shapes in a deterministic manner by mechanical buckling, with good reversibility and applicability to a variety of materials including inorganic semiconductors, metals, and polymers. One technical challenge, however, is in the assembly of complex 3D geometries that involve narrow regions of high strain, such as tightly foldable hinges, without damaging the

---

S. Lim, Y. Lee, Prof. J.-H. Ahn
School of Electrical and Electronic Engineering
Yonsei University
Seoul 03722, Republic of Korea
E-mail: ahnj@yonsei.ac.kr

Dr. H. Luan, S. Zhao, Prof. Y. Huang
Departments of Mechanical Engineering
Civil and Environmental Engineering
Materials Science and Engineering
Northwestern University
Evanston, IL 60208, USA
E-mail: y-huang@northwestern.edu

Dr. H. Luan, Prof. Y. Huang, Prof. J. A. Rogers
Querrey Simpson Institute for Bioelectronics
Northwestern University
Evanston, IL 60208, USA
E-mail: jrogers@northwestern.edu

The ORCID identification number(s) for the author(s) of this article can be found under https://doi.org/10.1002/adma.202001303.

S. Zhao
School of Aeronautic Science and Engineering
Beihang University
Beijing 100191, P. R. China

Prof. Y. Zhang
Applied Mechanics Laboratory
Department of Engineering Mechanics
Center for Flexible Electronics Technology
Tsinghua University
Beijing 100084, P. R. China

Prof. J. A. Rogers
Departments of Materials Science and Engineering
Biomedical Engineering
Neurological Surgery
Electrical and Computer Engineering
Mechanical Engineering
Chemistry
Northwestern University
Evanston, IL 60208, USA

DOI: 10.1002/adma.202001303

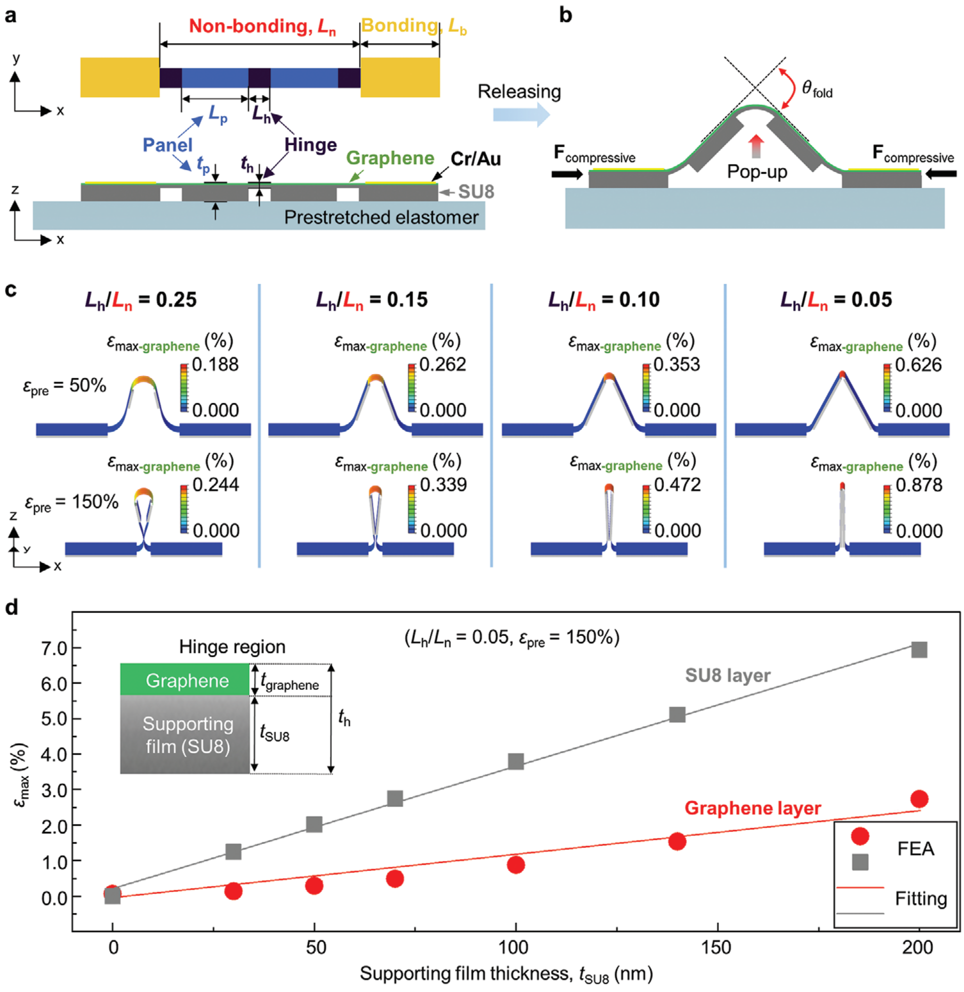

Figure 1. Schematic illustrations and FEA predictions for graphene-based 3D microstructures with sharp folds, formed by compressive buckling. a) Top view of origami designs for the 2D precursor. Cross-sectional view of the patterned 2D precursor on a prestretched substrate. b) Conceptual illustration of the folding mechanism during controlled buckling process. c) FEA results for achieving the smallest radius of curvature at the central hinge region by variations in the length ratio (L_h/L_n). Corresponding strain distribution in the graphene layer. d) FEA predictions of the maximum principal strain (ε_{max}) of graphene and SU8 layers for a fully folded structure as a function of supporting film thickness (t_{SU8}) at hinge region.

electrical and mechanical properties of the constituent materials and devices.

Herein, we introduce the 3D assembly of such classes of microstructures, leading to reversible 2D to 3D transformation of architectures that include sharp folds, without sacrificing the electrical properties. Here, graphene, formed by chemical vapor deposition (CVD), serves as an enabling conductive material at these hinge regions, due to its exceptional mechanical properties compared to those of conventional metals. Graphene hinges, owing to their good mechanical endurance, enable the reversible formation of multiple folded 3D structures from 2D precursors without compromising electrical performance. This approach offers significant possibilities for the development of transformable 3D systems while maintaining the initial functions even for high levels of deformation.

Figure 1 presents the design strategy for the 3D assembly of sharp folding microstructures via compressive buckling on a prestretched elastomer substrate. The 2D precursor, inspired by origami design,[33,36] comprises two areas, including the bonding pads (yellow color, length L_b), which strongly adhere to the elastomer substrate through surface chemical reactions, and the nonbonding regions (length L_n), which undergoes controlled compressive buckling to "pop-up" via physical separation from the substrate (Figure 1a). To provide appropriate spatial variations in the bending stiffness for sharp folding deformations, the nonbonding region is engineered to include reduced film thicknesses at selected segments (i.e., hinges). Specifically, flexible hinge regions (navy color, length L_h, thickness t_h) are thinner than rigid panel regions (blue color, length L_p, thickness t_p). Consequently, the low bending stiffnesses of the hinge regions lead to folding deformations via the compressive strain provided by the relaxation of the prestretched elastomer substrate. By comparison, the thick regions, with high bending stiffnesses, undergo negligible deformations. The folding angle (θ_{fold}) and bending radius of curvature (r) associated with the hinge regions can be controlled using variations of design parameters such as length ratio (L_h/L_n) and thickness ratio (t_h/t_p) of the hinge region to the nonbonding region (Figure 1a,b; Figure S1, Supporting Information).

The key design element of this foldable structure is the introduction of graphene (four layers grown via the CVD process). Because typical metals have low fracture strain and/or exhibit plasticity, they cannot serve as the basis for sharp folding structures capable of reversible 2D to 3D shape transformations (Figure S2, Supporting Information).[34,37] In contrast, graphene can maintain good electrical conductivity without experiencing mechanical and electrical failure under high strains,[38–44] thereby facilitating sharp folding. In the following, we present hinge structures composed of freestanding graphene and graphene supported by a thin layer of photocurable epoxy (SU8, ≤200 nm in thickness; other polymer materials with comparable mechanical and physical properties are also viable as supporting layers).

During the 2D to 3D geometry transformation, intensive folding deformations occur at the hinge regions. The maximum principal strains of the hinge during the transformation can be quantified through finite element analysis (FEA). Engineering the design of the hinge area plays an important role in reducing the strain level and avoiding mechanical fracture and electrical disconnection. As the length ratio (L_h/L_n) decreases for given conditions of thickness ratio ($t_h/t_p \approx 0.07$) and prestrain (ε_{pre} = 150%; corresponding to compressive strain $\varepsilon_{compr} = \varepsilon_{pre}/(1+\varepsilon_{pre})$ = 60%), the curvature radius of the folded region decreases and strain concentrations appear at the hinges (the evaluated strains on graphene and SU8 layers are in Figure 1c and Figure S3 (Supporting Information), respectively). When the length ratio is high ($L_h/L_n \approx 0.25$), the hinge region is slightly less folded, showing a large bending curvature radius ($r \approx 3.43$ µm) and a relatively low strain. On the other hand, a small length ratio ($L_h/L_n \approx 0.05$) enables sharp folding in a small curvature radius ($r \approx 1.16$ µm), which induces a relatively high level of strain as almost all the deformation is accommodated within the tiny hinges. Therefore, for sharp folding, special engineering considerations to avoid fracture are crucial. In addition, Figure S4 (Supporting Information) indicates that the threshold of thickness ratio t_h/t_p to realize sharp folding is ≈0.125, with the length factor $L_h/L_n = 0.05$ and prestrain level ε_{pre} = 150%.

Figure 1d depicts the maximum principal strain of the graphene and SU8 layers with respect to the thickness of the SU8 supporting layer in the hinge area. With a computational analysis tool based on FEA, the strain levels in both the graphene and SU8 layers are quantitatively accessible in all the hinge regions (Figures S5 and S6, Supporting Information). As the SU8 thickness (t_{SU8}) in the hinge area decreases for a fixed thickness of t_p (1.4 µm, in the panel area), the strain in the hinge induced by the relaxation of prestrain gradually decreases. The relatively thicker supporting film (t_{SU8} = 200 nm) leads to a higher strain (2.732% and 6.940% on graphene and SU8 layers, respectively), while a relatively thinner supporting film (≤100 nm) enables a lower strain (≤0.878% and ≤3.788%, respectively). Moreover, the maximum principal strain of the hinge comprising only graphene, without a supporting film, is much lower (by ≈1–2 orders of magnitude) than that of the hinge with the SU8 supporting layer, facilitating the design of multiple foldable structures.

Figure 2a–d shows the transformation process from 2D precursors to 3D-folded structures through controlled compressive buckling of thin films on prestretched elastomers and the experimentally achieved single-folded structures with three different hinge geometries of graphene/SU8 (1.34/100 nm, t_h = 101.34 nm), graphene/SU8 (1.34/50 nm, t_h = 51.34 nm), and graphene only (t_h = 1.34 nm), based on optimized design choices, respectively. The construction of sharp folded structures is challenging owing to the associated severe deformations. The thickness of the hinge regions was minimized to nanoscale via the introduction of graphene, decreasing the strain level and facilitating sharp folding. For a hinge thickness of t_h = 101.34 nm, as the prestrain of 150% fully releases, the folding angle of the hinge reaches its peak value, 180°, in agreement with FEA prediction. In addition, the FEA results indicate that the hinge deforms into a sharp arc shape, and the maximum principal strains ($\varepsilon_{max\text{-}graphene}$ = 0.878% and $\varepsilon_{max\text{-}SU8}$ = 3.788%) are far below the fracture strain thresholds (≈6%[18,45–47] and ≈11%,[11,48] respectively) of the constituent materials (Figure 2b; Figure S7, Supporting Information).

When the hinge thickness is reduced to t_h = 51.34 nm, the deformed shapes of the hinges become planar and a lower level of strain of $\varepsilon_{max\text{-}graphene}$ = 0.289% is induced in the graphene layer compared to that with t_h = 101.34 nm (Figure 2c). A further reduction of strain can be realized by using a freestanding graphene layer without the SU8. Figure 2d indicates that the shape of the folded hinge is flat, in contrast to the arc shapes of the cases with SU8. The freestanding graphene conformably covers the top of edge of the SU8 panels without material fracture, maintaining good electrical conductivity (Figure S8, Supporting Information) owing to its atomic-scale thickness. The graphene hinge with atomic-scale thickness undergoes negligible bending strain (≈6.373×10^{-2}%, from FEA considering only the folding process) during a large degree of folding, which enables the formation of deformed structures that exhibit extremely large deformations but maintain favorable electrical interconnectivity. The ratio of the thickness of the panel over the length of hinge t_p/L_h is another factor that influences the deformed shape of the hinge. When the ratio t_p/L_h increases toward 0.5, the hinge tends to flatten, with combined folding and stretching deformations, at a folding angle of ≈180° (Figure S9, Supporting Information).

This origami-inspired strategy of film thickness control of 2D precursors enables the construction of multiple-peak folded structures. **Figure 3** presents such structures achieved with 2D precursors using the graphene/SU8 supporting layer (1.34/100 nm, t_h = 101.34 nm) and only graphene (t_h = 1.34 nm) in the hinge areas. Figure 3a and Figure S10 (Supporting Information) show the 2D precursor of a multiple-peak foldable structure that includes five hinges, the resulting 3D structure, and the folding mechanism. Two bonding pads at the ends (yellow) adhere strongly to a uniaxially prestrained substrate, whereas all the other regions (except the central hinge) of the 2D precursors release from the substrate and folding deformations in the hinges occur through the prestrain relief. The prestrain required for the formation of the multiple foldable structure depends on the size of bonding pads (Figure S11a,b, Supporting Information). As the sizes of the bonding pads increase, the required prestrains decrease, whereas long bonding pads need to have a moderate stiffness (e.g., by adjusting the thickness of the pads) to prevent themselves from buckling/wrinkling and from inducing high interfacial stresses

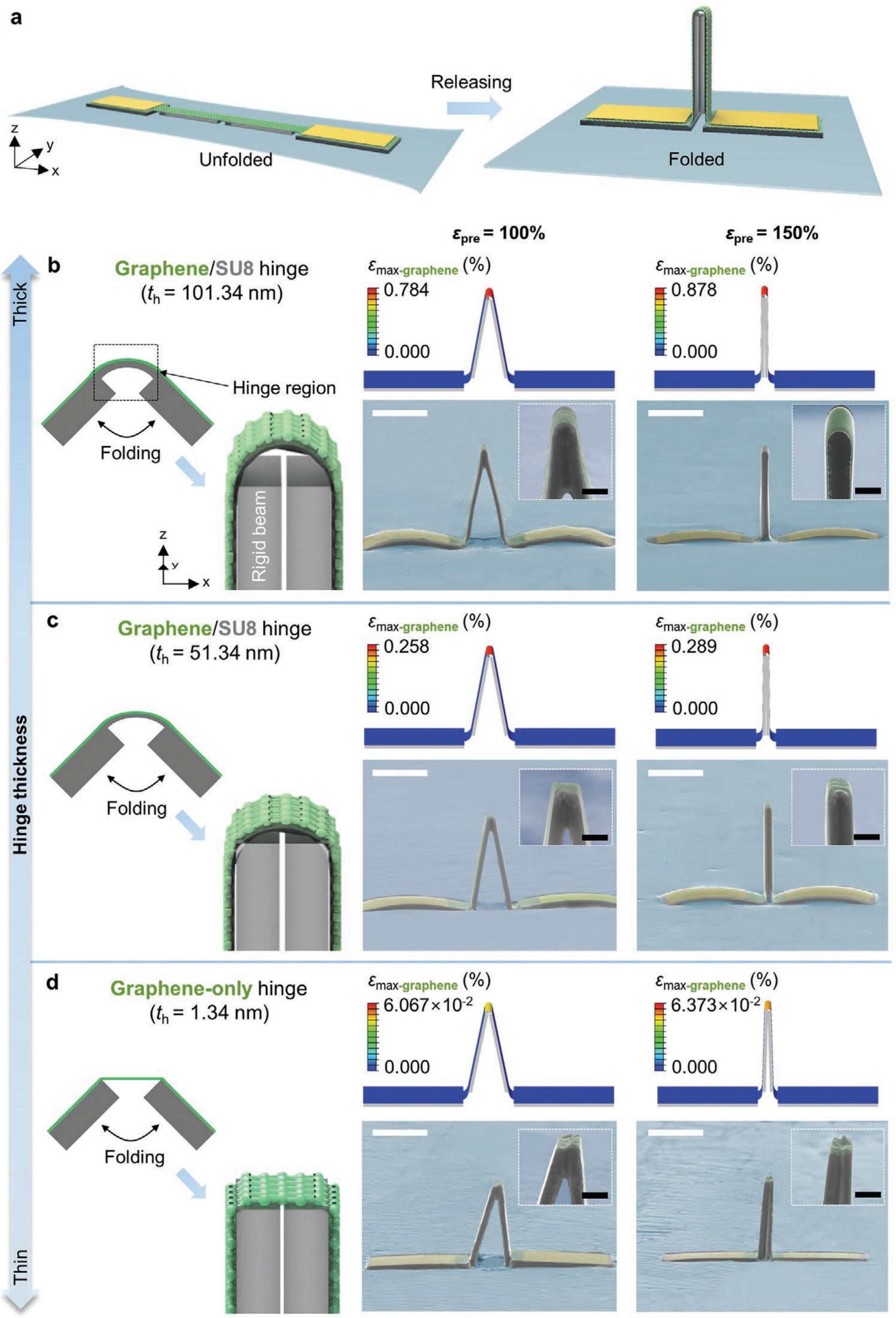

Figure 2. FEA results and corresponding SEM images of folded structures with different hinge thicknesses. a) Schematic illustration of concepts for 3D assembly of single-folded structures formed via compressive buckling. b–d) Conceptual illustrations of the folding behavior at the central hinge region. FEA results to evaluate the maximum principal strain distributions in the graphene layer. SEM images showing changes in the 3D structures depending on the variation of hinge thickness. Three different thicknesses for the hinge regions: b) graphene (1.34 nm)/SU8 (100 nm), c) graphene (1.34 nm)/SU8 (50 nm), and d) graphene-only (1.34 nm). Scale bar, 20 µm in white color, and 3 µm in black color.

that could lead to delamination. Design considerations on the geometry and stiffness of the bonding pads are particularly important to avoid delamination from the elastomer substrate in the context of cyclic loads. The 2D precursor design is optimized based on the FEA results (Figure S12a, Supporting Information). Both the experimental and FEA results show that each 3D structure first forms double triangles and then evolves to a compact folded shape with four panels aligning seamlessly in sequence as the 3D assembly progress proceeds. The FEA predictions of the multiple-peak 3D structure at different

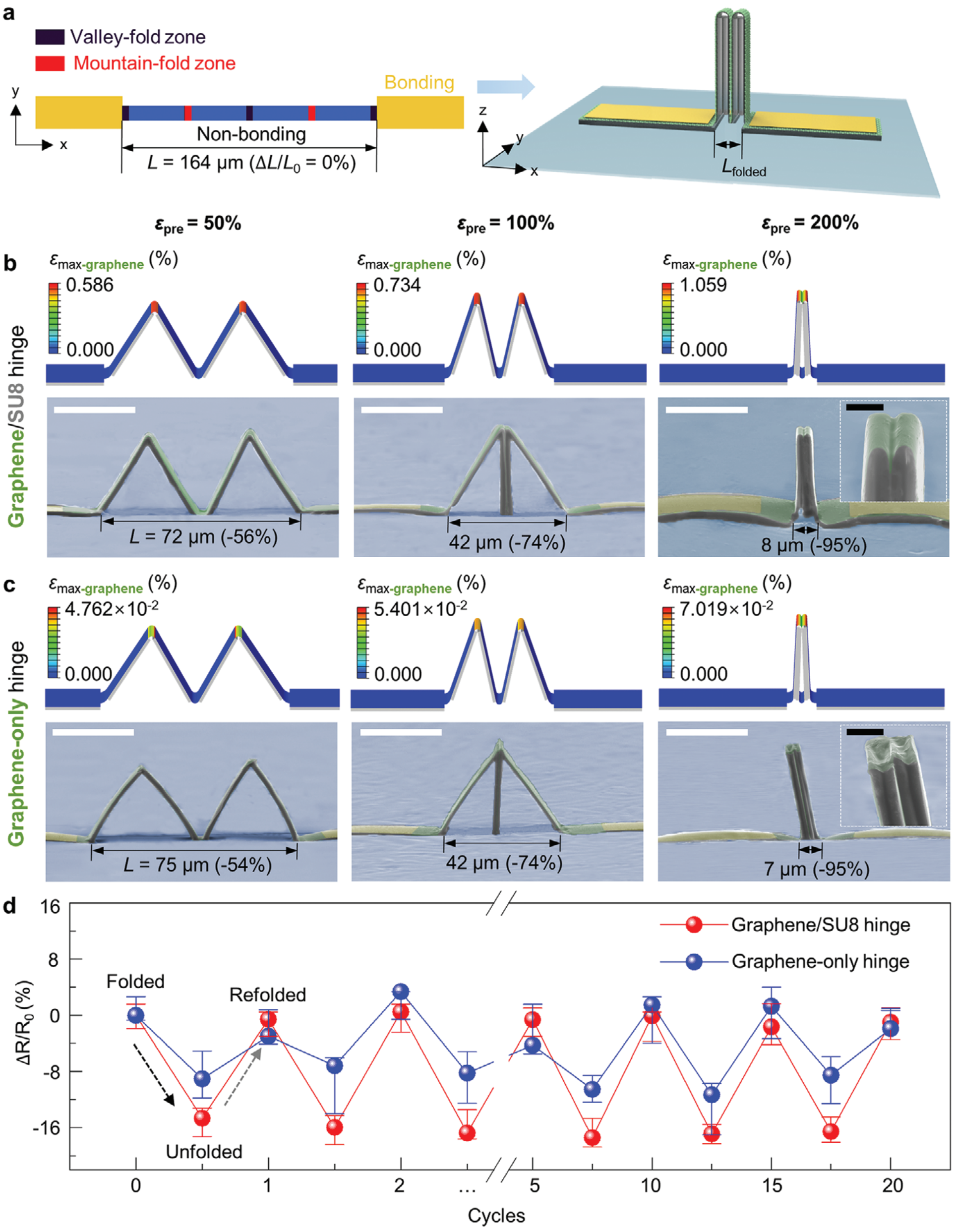

Figure 3. 3D microstructures with valley-fold hinges and mountain-fold hinges to access geometries that minimize the edge-to-edge length along the base (L). a) Schematic illustrations of a 2D precursor and a fully folded 3D shape. b,c) FEA results of the distribution of maximum principal strain in the graphene layer and corresponding SEM images of multiple folded structures under three different prestrain levels (scale bar, 30 µm in white, and 4 µm in black). d) Experimental results of the reversible behavior of relative resistance change in cyclic test for multiple folded structures (black and gray colors denote the stretching and releasing operation, respectively, under 200% prestrain).

prestrains (50%, 100%, and 200%) correspond to the experimental results observed via a scanning electron microscopy (SEM) (Figure 3b,c). The slightly inclining geometry of the 3D origami shape may arise from unbalanced adhesion of the hinges on the two sides to the elastomer substrate or to the 3D structure itself through van der Waals forces. The maximum principal strains ($\varepsilon_{\text{max-graphene}}$ = 1.059% and $\varepsilon_{\text{max-SU8}}$ = 8.136%; Figure 3b; Figure S13a, Supporting Information), according to FEA results (red color), localize at the hinge but remain below the fracture thresholds of graphene and SU8 epoxy. The hinge consisting only of graphene, without the SU8 supporting layer, induces very low strain ($\approx 7.019 \times 10^{-2}$%, from FEA considering only the folding process), allowing graphene to cover the edge of the rigid beams. The transformation processes from 2D to 3D on elastomer substrates are reversible without mechanical and electrical failure. These 3D structures allow the minimization of interconnect length owing to its multiple folding behaviors ($\Delta L/L_0 \approx -95\%$, inset in the SEM images). Such advantages open the possibility of developing extremely compact, yet fully functional, devices. In cyclic stretching tests (Figure 3d), graphene showed stable electrical conductivity without any failure, exhibiting repetitive up and down variations of resistance with

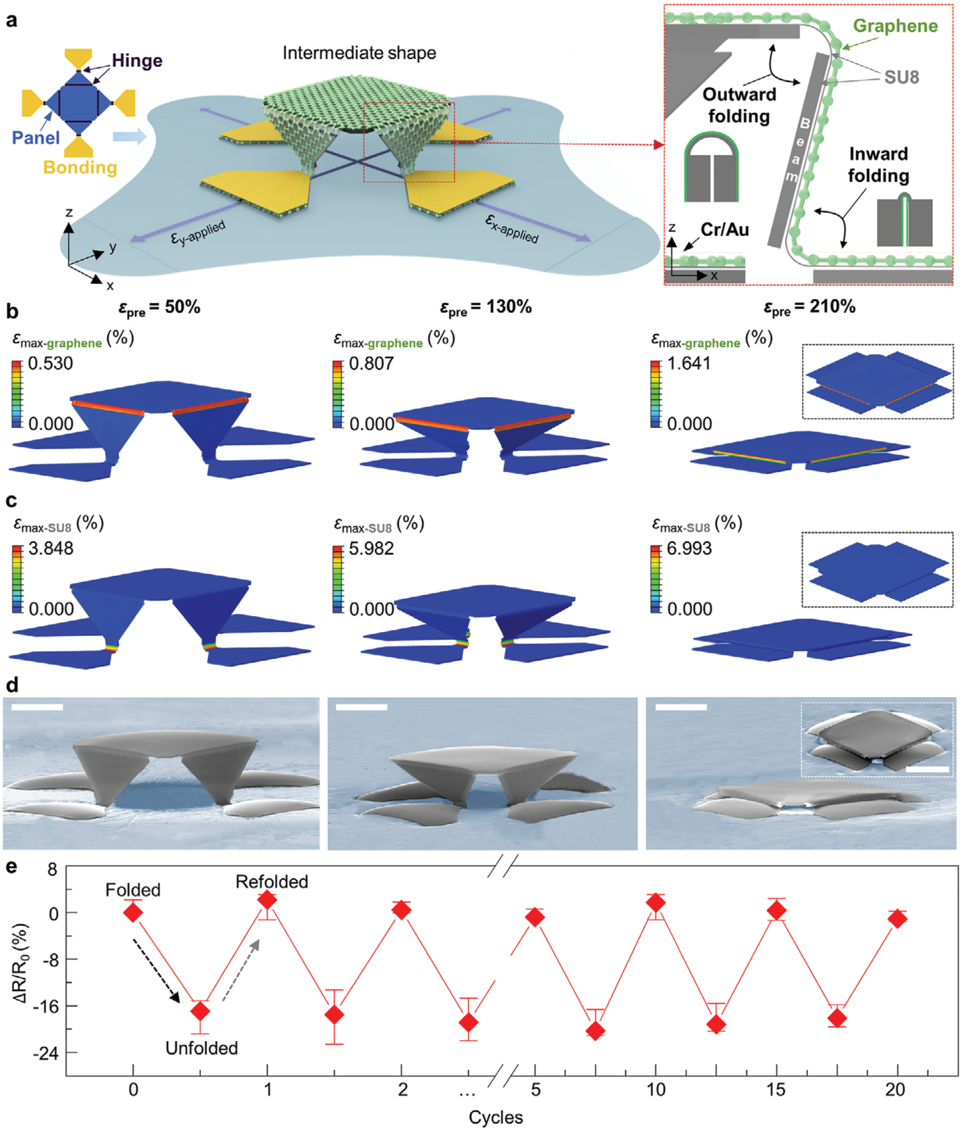

Figure 4. Development of table-shaped foldable 3D microstructure based on simultaneously inward and outward folding deformations under biaxial compressive strain. a) Schematic illustration of a 2D precursor and an intermediate 3D shapes. Cross-sectional view of two different folding mechanisms depending on the position of the hinge film. b,c) FEA results for strain distributions in the graphene layer (b) and the SU8 layer (c). d) Corresponding SEM images of deformed shapes under three different prestrain levels (scale bar, 40 µm). e) Measurement results of the relative resistance change in a cyclic test of the table-shaped 3D structure (black and gray colors denote the stretching and releasing operation, respectively, under 210% prestrain).

folding and unfolding, respectively. Folded 3D structures show higher resistances than those of unfolded 2D shapes by ≈16.7% because the graphene in the hinge is subjected to a relatively high strain (≈1.059%). Compared with the graphene/SU8 hinge, the graphene-only hinge induces a much lower strain, and a smaller variation in resistance is expected. Despite this expectation, the two types of hinge exhibit similar variation. We speculate that the graphene around the edges of the beam undergoes large deformations locally (e.g., wrapping of graphene layer around the edge resulted from interfacial adhesion, and possibly relative slip between graphene and SU8 layers), leading to large changes in resistance.

A diverse range of 3D geometries is accessible using equally biaxial prestrain. As a representative example, a table-shaped foldable structure comprising one square, four triangles, and four bonding pads was demonstrated via biaxial compression (**Figure 4**). In the 2D layout of the precursor (Figures S11c and S12b, Supporting Information), the patterns of the hinge and the bonding locations of the pads provide important means to construct the final 3D geometries. During assembly, the regions of the surface square undergo negligible deformations, such that the compressive strains are accommodated by the four legs of the triangle shape. The table rises to the highest position under the release of prestrain of 50% and subsequently collapses to the substrate as the compressive strain further increases. To achieve this deformation behavior, the table structure here is designed to have different folding mechanisms, with inward and outward foldings according to the relative position of the compliant hinge regions to the rigid panel regions (Figure 4a). The films of the hinge area include graphene on top and SU8 as a bottom layer (1.34/140 nm, $t_h = 141.34$ nm). Thereby, the maximum tensile strain of graphene layer ($\varepsilon_{max} = 1.641\%$, Figure 4b) occurs at the outward folding regions (at the upper part of legs), whereas that of SU8 layer ($\varepsilon_{max} = 6.993\%$, Figure 4c) occurs at the inward folding regions (at the lower part of legs). The folded hinge in the table structure induces a relatively higher tensile strain than that associated with other structures. As a result, a relatively higher variation of ≈20.2% in resistance occurs upon folding and unfolding. However, this 3D graphene/SU8 table structure maintains elastic deformations with strains below the fracture thresholds of constituent materials. In cyclic biaxial stretching tests (Figure 4e), the graphene layer on folded and unfolded objects shows stable electrical conductivity without any disconnection.

We introduce assembly and design principles for the formation of conductive, foldable 3D structures using graphene as an engineered hinge, capable of operating in a continuous and reversible manner. Atomically thin graphene effectively reduces the maximum strain in the hinge region during the controlled compressive buckling that initiates a geometric transformation of a 2D precursor into a 3D microstructure, and the 3D system maintains stable electrical conductivity without failure under high levels of deformation, including those associated with 180° sharp folds. Based on experimental and computational analyses, complex 3D structures such as multiple folded and table shapes were demonstrated. This approach, combined with the graphene hinge, provides a promising route for advanced electronic devices with unconventional engineering designs, such as foldable smartphones and displays, and challenging and sophisticated devices that embrace micro/nanoscale dimensions, such as 3D photodetectors and biosensors. In addition, the architecture of the 3D structures could apply to other atomic-scale materials such as transition metal dichalcogenides and ultrathin perovskites for electronics in unusual formats. Practical implementation of 3D techniques involves considerable challenges, including the enhancement of bonding strengths between active materials and supporting polymers, the improvement of the environmental stability of 3D structures against moisture and chemicals in the air, and a method to decrease defects, such as cracks. Resolving these challenges will facilitate the realization for emerging electronics with new functionalities.

Experimental Section

Finite Element Analysis: 3D FEA was performed in software suite Abaqus FEA to analyze the nonlinear mechanical behaviors of 2D precursors and elastomer substrates. Eight-node solid elements and four-node shell elements were used for the substrates and the 2D precursors, respectively. The mesh size was tested for convergence to ensure computational accuracy. Linear buckling analysis for the 2D precursors under compression was conducted to determine the critical buckling strain and corresponding buckling mode, which were then considered as initial geometric imperfections in postbuckling analysis. The deformed 3D shapes and strain distributions at different prestrains for the 2D precursors can be obtained through the postbuckling analysis. SU8 epoxy was modeled as a linear elastic material with a Young's modulus of $E_{SU8} = 4.02$ GPa and a Poisson's ratio of $\nu_{SU8} = 0.22$. Graphene (four layers) was simulated as linear elastic with an in-plane Young's modulus of $E_{graphene} = 1.26$ TPa and a Poisson's ratio of $\nu_{graphene} = 0.24$. The substrate material (Dragon Skin 10) was simulated as an incompressible Mooney–Rivlin solid, with an elastic modulus of $E_{DragonSkin} = 166$ kPa.

Fabrication of Foldable 3D Microstructures Based on Graphene: The 3D assembly here followed a typical compressive force-driven buckling method, as illustrated in Figure S14 (Supporting Information). The pattern design of the 2D precursors was inspired by an optimized origami design according to the desired 3D microstructures. First, Cr/Au contact pads (5/45 nm) for electrical measurement were patterned on a SiO_2/Si wafer via thermal evaporation and conventional photolithography methods. After transferring graphene (four layers ≈ 1.34 nm; Figure S15, Supporting Information), which was grown by conventional CVD process and produced by a layer-by-layer stacking method, to the substrates through wet transfer, the graphene film was developed via lithography and reactive ion etching with O_2 plasma (40 sccm, 100 W, 10 s). Four-layer graphene was used for stable electrical properties without mechanical failure because multilayer stacked graphene can compensate for the defects created by synthesis and transfer processes. This patterned graphene was used as a component for the electrical connection. For the graphene/SU8 hinge-based 2D precursor, the thin SU8 layer (≤200 nm, diluted SU8 2000.5 with ≈72 vol% SU8 2000 thinner) as a flexible hinge was spin-coated and patterned first, and the thick SU8 layer (≈1.4 µm, SU8 2002 was spin-coated at ≈6000 rpm) as rigid panels was subsequently defined in a similar manner. The graphene-only hinge-based the 2D precursor was defined as the graphene layer without a supporting film layer in the hinge regions (thick SU8 layer was used as rigid panels). After patterning the 2D precursor, the buried SiO_2 layer was shifted slightly to the edges of this 2D precursor through immersion in buffered oxide etchant (BOE). In the next process of fully removing the SiO_2 layer via hydrofluoric acid (HF) treatment, the photoresist (PR) cover layer (≈1.14 µm, AZ5214-E Photoresist, MERCK) protected the graphene-based 2D precursor. The techniques of transfer using a polydimethylsiloxane (PDMS)-based stamp (Sylgard 184, Dow corning) and polyvinyl alcohol (PVA) tape (water-soluble purge tape, AQUASOL) facilitated the delivery of the fabricated 2D precursor to prestretched ($\varepsilon_{pre} \leq 210\%$) elastomer substrate (Dragon Skin 10, Smooth-On). After UV–ozone exposure and baking, the fabricated 2D precursor on PVA tape was laminated stably onto the prestretched elastomer substrate. After dissolving the PVA tape and PR cover layer by using deionized (DI) water and acetone, respectively, the nonbonding regions, which were slightly separated from the elastomer substrate, were folded based on the hinge area via the out-of-plane compressive force that occurred under relaxing operations of the prestretched elastomer substrate. These optimized processes enabled a stable folding behavior of graphene-based origami structure during 3D assembly.

Supporting Information

Supporting Information is available from the Wiley Online Library or from the author.

Acknowledgements

S.L. and H.L. contributed equally to this work. This work was supported by the National Research Foundation of Korea (NRF) funded by the Korean government (MSIT) (NRF-2015R1A3A2066337). Y.Z. acknowledges the support from the National Natural Science Foundation of China (Grant No. 11722217) and the Tsinghua National Laboratory for Information Science and Technology. Y.H. acknowledges the support from the National Science Foundation (Grant No. CMMI1635443). J.A.R. acknowledges support from the Army Research Office through an Award No. W911NF-17-1-0351.

Conflict of Interest

The authors declare no conflict of interest.

Keywords

3D assembly, compressive buckling, foldable structures, graphene, origami

Received: February 24, 2020
Revised: April 23, 2020

---

[1] A. C. Siegel, S. T. Phillips, M. D. Dickey, N. Lu, Z. Suo, G. M. Whitesides, *Adv. Funct. Mater.* **2010**, *20*, 28.

[2] S. A. Zotov, M. C. Rivers, A. A. Trusov, A. M. Shkel, *IEEE Sens. J.* **2011**, *11*, 2780.

[3] S. Felton, M. Tolley, E. Demaine, D. Rus, R. Wood, *Science* **2014**, *345*, 644.

[4] B. H. Kim, J. Lee, S. M. Won, Z. Xie, J.-K. Chang, Y. Yu, Y. K. Cho, H. Jang, J. Y. Jeong, Y. Lee, A. Ryu, D. H. Kim, K. H. Lee, J. Y. Lee, F. Liu, X. Wang, Q. Huo, S. Min, D. Wu, B. Ji, A. Banks, J. Kim, N. Oh, H. M. Jin, S. Han, D. Kang, C. H. Lee, Y. M. Song, Y. Zhang, Y. Huang, K.-I. Jang, J. A. Rogers, *ACS Nano* **2018**, *12*, 4164.

[5] M. Han, H. Wang, Y. Yang, C. Liang, W. Bai, Z. Yan, H. Li, Y. Xue, X. Wang, B. Akar, H. Zhao, H. Luan, J. Lim, I. Kandela, G. A. Ameer, Y. Zhang, Y. Huang, J. A. Rogers, *Nat. Electron.* **2019**, *2*, 26.

[6] D. Bishop, F. Pardo, C. Bolle, R. Giles, V. Aksyuk, *J. Low Temp. Phys.* **2012**, *169*, 386.

[7] J. Rogers, Y. Huang, O. G. Schmidt, D. H. Gracias, *MRS Bull.* **2016**, *41*, 123.

[8] X. Ning, H. Wang, X. Yu, J. A. N. T. Soares, Z. Yan, K. Nan, G. Velarde, Y. Xue, R. Sun, Q. Dong, H. Luan, C. M. Lee, A. Chempakasseril, M. Han, Y. Wang, L. Li, Y. Huang, Y. Zhang, J. A. Rogers, *Adv. Funct. Mater.* **2017**, *27*, 1605914.

[9] X. Ning, X. Yu, H. Wang, R. Sun, R. E. Corman, H. Li, C. M. Lee, Y. Xue, A. Chempakasseril, Y. Yao, Z. Zhang, H. Luan, Z. Wang, W. Xia, X. Feng, R. H. Ewoldt, Y. Huang, Y. Zhang, J. A. Rogers, *Sci. Adv.* **2018**, *4*, eaat8313.

[10] X. Wang, X. Guo, J. Ye, N. Zheng, P. Kohli, D. Choi, Y. Zhang, Z. Xie, Q. Zhang, H. Luan, K. Nan, B. H. Kim, Y. Xu, X. Shan, W. Bai, R. Sun, Z. Wang, H. Jang, F. Zhang, Y. Ma, Z. Xu, X. Feng, T. Xie, Y. Huang, Y. Zhang, J. A. Rogers, *Adv. Mater.* **2019**, *31*, 1805615.

[11] W. Pang, X. Cheng, H. Zhao, X. Guo, Z. Ji, G. Li, Y. Liang, Z. Xue, H. Song, F. Zhang, Z. Xu, L. Sang, W. Huang, T. Li, Y. Zhang, *Natl. Sci. Rev.* **2020**, *7*, 342.

[12] Z. Song, T. Ma, R. Tang, Q. Cheng, X. Wang, D. Krishnaraju, R. Panat, C. K. Chan, H. Yu, H. Jiang, *Nat. Commun.* **2014**, *5*, 3140.

[13] Z. Song, X. Wang, C. Lv, Y. An, M. Liang, T. Ma, D. He, Y.-J. Zheng, S.-Q. Huang, H. Yu, H. Jiang, *Sci. Rep.* **2015**, *5*, 10988.

[14] C. L. Randall, E. Gultepe, D. H. Gracias, *Trends Biotechnol.* **2012**, *30*, 138.

[15] V. A. Bolaños Quiñones, H. Zhu, A. A. Solovev, Y. Mei, D. H. Gracias, *Adv. Biosyst.* **2018**, *2*, 1800230.

[16] A. Lamoureux, K. Lee, M. Shlian, S. R. Forrest, M. Shtein, *Nat. Commun.* **2015**, *6*, 8092.

[17] K. Zhang, Y. H. Jung, S. Mikael, J.-H. Seo, M. Kim, H. Mi, H. Zhou, Z. Xia, W. Zhou, S. Gong, Z. Ma, *Nat. Commun.* **2017**, *8*, 1782.

[18] W. Lee, Y. Liu, Y. Lee, B. K. Sharma, S. M. Shinde, S. D. Kim, K. Nan, Z. Yan, M. Han, Y. Huang, Y. Zhang, J.-H. Ahn, J. A. Rogers, *Nat. Commun.* **2018**, *9*, 1417.

[19] W. Xu, T. Li, Z. Qin, Q. Huang, H. Gao, K. Kang, J. Park, M. J. Buehler, J. B. Khurgin, D. H. Gracias, *Nano Lett.* **2019**, *19*, 7941.

[20] C. Py, P. Reverdy, L. Doppler, J. Bico, B. Roman, C. N. Baroud, *Phys. Rev. Lett.* **2007**, *98*, 156103.

[21] M. K. Blees, A. W. Barnard, P. A. Rose, S. P. Roberts, K. L. McGill, P. Y. Huang, A. R. Ruyack, J. W. Kevek, B. Kobrin, D. A. Muller, P. L. McEuen, *Nature* **2015**, *524*, 204.

[22] A. Cui, Z. Liu, J. Li, T. H. Shen, X. Xia, Z. Li, Z. Gong, H. Li, B. Wang, J. Li, H. Yang, W. Li, C. Gu, *Light: Sci. Appl.* **2015**, *4*, e308.

[23] D. Joung, A. Nemilentsau, K. Agarwal, C. Dai, C. Liu, Q. Su, J. Li, T. Low, S. J. Koester, J.-H. Cho, *Nano Lett.* **2017**, *17*, 1987.

[24] M. Z. Miskin, K. J. Dorsey, B. Bircan, Y. Han, D. A. Muller, P. L. McEuen, I. Cohen, *Proc. Natl. Acad. Sci. USA* **2018**, *115*, 466.

[25] E. Hawkes, B. An, N. M. Benbernou, H. Tanaka, S. Kim, E. D. Demaine, D. Rus, R. J. Wood, *Proc. Natl. Acad. Sci. USA* **2010**, *107*, 12441.

[26] J.-H. Cho, M. D. Keung, N. Verellen, L. Lagae, V. V. Moshchalkov, P. Van Dorpe, D. H. Gracias, *Small* **2011**, *7*, 1943.

[27] W. J. Arora, A. J. Nichol, H. I. Smith, G. Barbastathis, *Appl. Phys. Lett.* **2006**, *88*, 053108.

[28] N. Bassik, G. M. Stern, D. H. Gracias, *Appl. Phys. Lett.* **2009**, *95*, 091901.

[29] T. Deng, C. Yoon, Q. Jin, M. Li, Z. Liu, D. H. Gracias, *Appl. Phys. Lett.* **2015**, *106*, 203108.

[30] Y. Zhang, F. Zhang, Z. Yan, Q. Ma, X. Li, Y. Huang, J. A. Rogers, *Nat. Rev. Mater.* **2017**, *2*, 17019.

[31] S. Xu, Z. Yan, K.-I. Jang, W. Huang, H. Fu, J. Kim, Z. Wei, M. Flavin, J. McCracken, R. Wang, A. Badea, Y. Liu, D. Xiao, G. Zhou, J. Lee, H. U. Chung, H. Cheng, W. Ren, A. Banks, X. Li, U. Paik, R. G. Nuzzo, Y. Huang, Y. Zhang, J. A. Rogers, *Science* **2015**, *347*, 154.

[32] Y. Zhang, Z. Yan, K. Nan, D. Xiao, Y. Liu, H. Luan, H. Fu, X. Wang, Q. Yang, J. Wang, W. Ren, H. Si, F. Liu, L. Yang, H. Li, J. Wang, X. Guo, H. Luo, L. Wang, Y. Huang, J. A. Rogers, *Proc. Natl. Acad. Sci. USA* **2015**, *112*, 11757.

[33] Z. Yan, F. Zhang, J. Wang, F. Liu, X. Guo, K. Nan, Q. Lin, M. Gao, D. Xiao, Y. Shi, Y. Qiu, H. Luan, J. H. Kim, Y. Wang, H. Luo, M. Han, Y. Huang, Y. Zhang, J. A. Rogers, *Adv. Funct. Mater.* **2016**, *26*, 2629.

[34] Y. Shi, F. Zhang, K. Nan, X. Wang, J. Wang, Y. Zhang, Y. Zhang, H. Luan, K.-C. Hwang, Y. Huang, J. A. Rogers, Y. Zhang, *Extreme Mech. Lett.* **2017**, *11*, 105.

[35] M. Humood, Y. Shi, M. Han, J. Lefebvre, Z. Yan, M. Pharr, Y. Zhang, Y. Huang, J. A. Rogers, A. A. Polycarpou, *Small* **2018**, *14*, 1703852.

[36] E. A. P. Hernandez, D. J. Hartl, D. C. Lagoudas, *Active Origami: Modeling, Design, and Applications*, Springer International Publishing, Cham, Switzerland **2018**.

[37] J.-H. Ahn, J. H. Je, *J. Phys. D: Appl. Phys.* **2012**, *45*, 103001.

[38] K. S. Kim, Y. Zhao, H. Jang, S. Y. Lee, J. M. Kim, K. S. Kim, J.-H. Ahn, P. Kim, J.-Y. Choi, B. H. Hong, *Nature* **2009**, *457*, 706.

[39] Y. Lee, S. Bae, H. Jang, S. Jang, S.-E. Zhu, S. H. Sim, Y. I. Song, B. H. Hong, J.-H. Ahn, *Nano Lett.* **2010**, *10*, 490.

[40] S. Bae, H. Kim, Y. Lee, X. Xu, J.-S. Park, Y. Zheng, J. Balakrishnan, T. Lei, H. Ri Kim, Y. I. Song, Y.-J. Kim, K. S. Kim, B. Özyilmaz, J.-H. Ahn, B. H. Hong, S. Iijima, *Nat. Nanotechnol.* **2010**, *5*, 574.

[41] X.-W. Fu, Z.-M. Liao, J.-X. Zhou, Y.-B. Zhou, H.-C. Wu, R. Zhang, G. Jing, J. Xu, X. Wu, W. Guo, D. Yu, *Appl. Phys. Lett.* **2011**, *99*, 213107.

[42] J. Zhao, C. He, R. Yang, Z. Shi, M. Cheng, W. Yang, G. Xie, D. Wang, D. Shi, G. Zhang, *Appl. Phys. Lett.* **2012**, *101*, 063112.

[43] S.-H. Bae, Y. Lee, B. K. Sharma, H.-J. Lee, J.-H. Kim, J.-H. Ahn, *Carbon* **2013**, *51*, 236.

[44] S. Won, Y. Hwangbo, S.-K. Lee, K.-S. Kim, K.-S. Kim, S.-M. Lee, H.-J. Lee, J.-H. Ahn, J.-H. Kim, S.-B. Lee, *Nanoscale* **2014**, *6*, 6057.

[45] R. Grantab, V. B. Shenoy, R. S. Ruoff, *Science* **2010**, *330*, 946.

[46] G.-H. Lee, R. C. Cooper, S. J. An, S. Lee, A. van der Zande, N. Petrone, A. G. Hammerberg, C. Lee, B. Crawford, W. Oliver, J. W. Kysar, J. Hone, *Science* **2013**, *340*, 1073.

[47] P. Zhang, L. Ma, F. Fan, Z. Zeng, C. Peng, P. E. Loya, Z. Liu, Y. Gong, J. Zhang, X. Zhang, P. M. Ajayan, T. Zhu, J. Lou, *Nat. Commun.* **2014**, *5*, 3782.

[48] T. Xu, J. H. Yoo, S. Babu, S. Roy, J.-B. Lee, H. Lu, *J. Micromech. Microeng.* **2016**, *26*, 105001.

ADVANCED
MATERIALS

Supporting Information

for *Adv. Mater.*, DOI: 10.1002/adma.202001303

Assembly of Foldable 3D Microstructures Using Graphene Hinges

Seungyun Lim, Haiwen Luan, Shiwei Zhao, Yongjun Lee, Yihui Zhang, Yonggang Huang, John A. Rogers,* and Jong-Hyun Ahn**

Supporting Information

Assembly of Foldable 3D Microstructures Using Graphene Hinges

Seungyun Lim, Haiwen Luan, Shiwei Zhao, Yongjun Lee, Yihui Zhang, Yonggang Huang, John A. Rogers and Jong-Hyun Ahn

Definition of sharp folding deformation in mechanically-guided 3D assembly. In the mechanically-driven 3D assembly, 'sharp folding' is defined as a sharp curvature-induced bending motion with almost straight folding line generated by using narrow creases (i.e., hinges). To achieve such deformation in 3D structures, specialized engineering designs for the 2D precursors are required, since the fundamental mechanism for 3D origami depends on the compressive strain provided by the relaxation of prestrain ($\varepsilon_{\mathrm{pre}}$) in an elastomeric substrate. For sharp folding motions, conditions such as a large folding angle, flat thickened regions (i.e., panels and bonding pads) and a small radius of curvature (at the hinge) are preferred. The deformed shape of the origami structure is influenced by the length and thickness factors in selected regions of the 2D precursor. Figure S1 indicates FEA predictions for sharp folding motions with variations of design parameters such as length ratio and thickness ratio of the hinge region to the non-bonding region. With a sufficiently small thickness ratio (thin/thick), the bending stiffness (relative stiffness $\propto E w_{\mathrm{i}} t_{\mathrm{i}}^{3} / L_{\mathrm{i}}$, for a single constituent material, where E is the elastic modulus, and w_{i}, t_{i}, and L_{i} are the width, thickness and length of each segment, respectively) of the hinge remains much smaller than that of the thick regions, so that these thick regions undergo negligible deformation. By using the following geometric relation,

$$\frac{L_1/L_{\mathrm{n}} + 2L_2/L_{\mathrm{n}}}{\theta_{\mathrm{fold}}} \sin\frac{\theta_{\mathrm{fold}}}{2} + \frac{L_{\mathrm{n}} - L_1 - 2L_2}{2L_{\mathrm{n}}} \cos\frac{\theta_{\mathrm{fold}}}{2} + L_{\mathrm{b}}/2L_{\mathrm{n}} = \frac{1 + L_{\mathrm{b}}/L_{\mathrm{n}}}{2(1+\varepsilon_{\mathrm{pre}})} \qquad (1)$$

we can predict the folding angle (θ_{fold}) and normalized radius of curvature (R_c^*) as a function of the prestrain ($\varepsilon_{\mathrm{pre}}$), for a given thickness factor ($t_{\mathrm{h}}/t_{\mathrm{n}} = 0.05$). These results imply that the length (L_1) and thickness (t_{h}) of a central hinge region influences the radius of curvature and strain level in the sharp folding deformation. The computational analysis (e.g., FEA) is essential in designing and forming sharp folding structures in a practical and reliable manner. Based on a guideline established by these FEA predictions, we achieved sharp folding structures, which result in folding angles of ≈180°, via controlled buckling-driven 3D assembly.

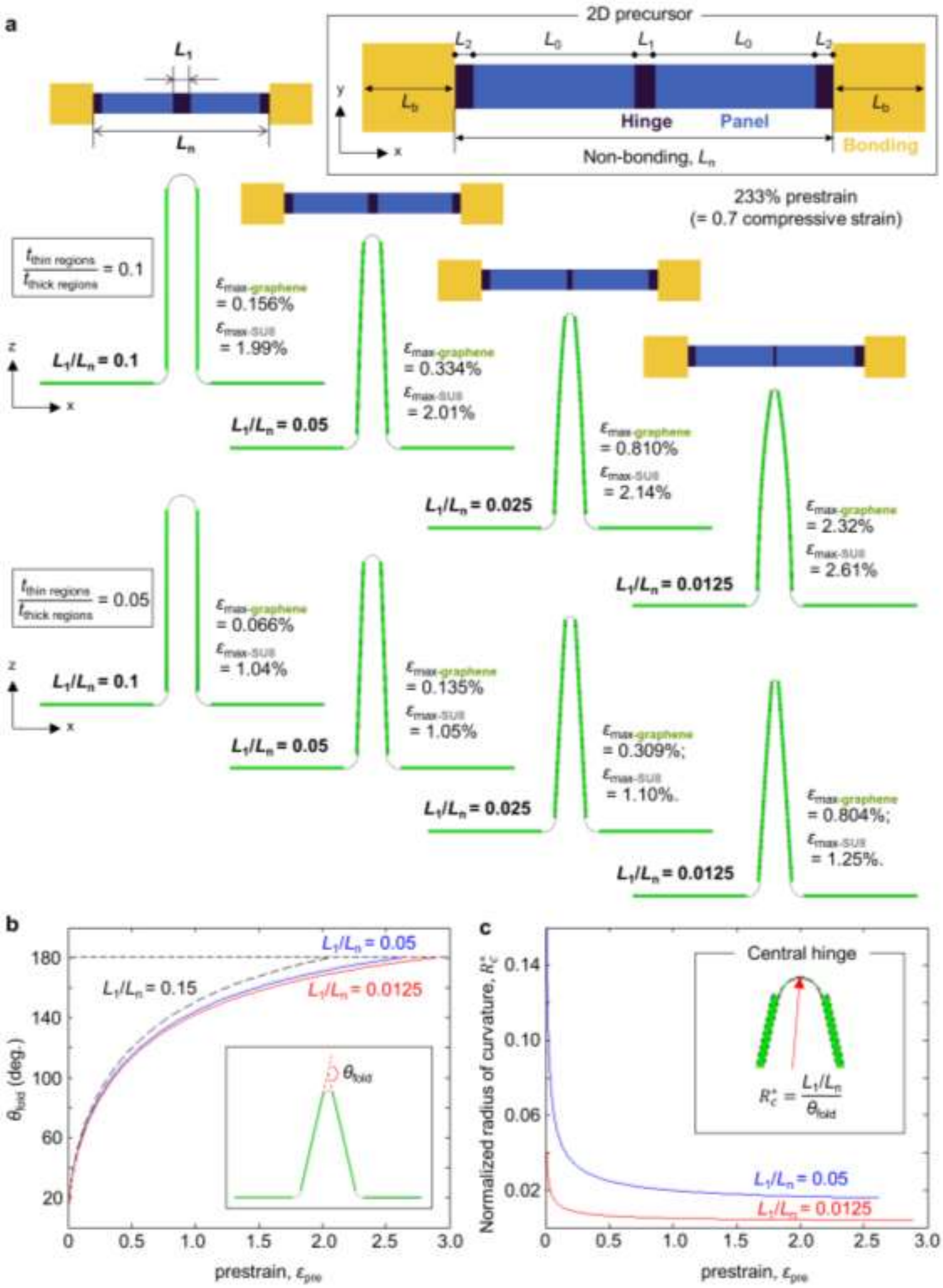

Figure S1. Influence of the normalized length ratio (L_1/L_n) on the central hinge in 3D origami structures. a) FEA predictions of the deformed shape of 3D origami structures influenced by the length ratio or thickness ratio. Four different length ratios (L_1/L_n) of 0.1, 0.05, 0.025, 0.0125, for two different thickness ratios (t_h/t_n) of 0.1 (0.05/0.5 μm) and 0.05 (0.025/0.5 μm). b)-c) FEA results of folding angle (θ_{fold}) and normalized radius of curvature (R_c^*) as a function of the prestrain ($\varepsilon_{\mathrm{pre}}$) by the analytic relation (1), in given conditions of $L_2/L_n = 0.05$ and $L_b/L_n = 0.25$.

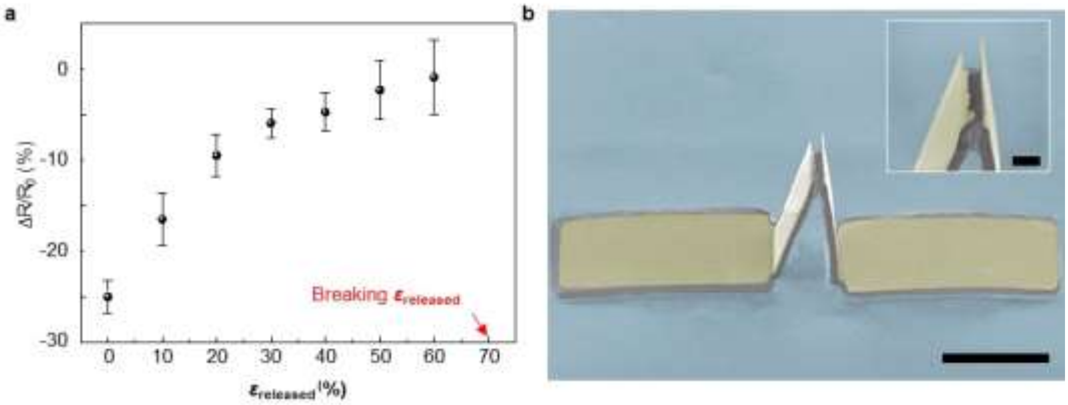

Figure S2. Fractional change in resistance as a function of released strain and colorized SEM image of a folded structure with Cr (5 nm)/Au (50 nm) as the hinge. a) The change of relative electrical resistance for such a folded structure as strain releases from a prestrain of 150%. The metal hinge fractures at a release of ~70 %, b) SEM image of the broken metal hinge. Scale bars, 20 µm and 3 µm (inset). (yellow color indicates Cr/Au).

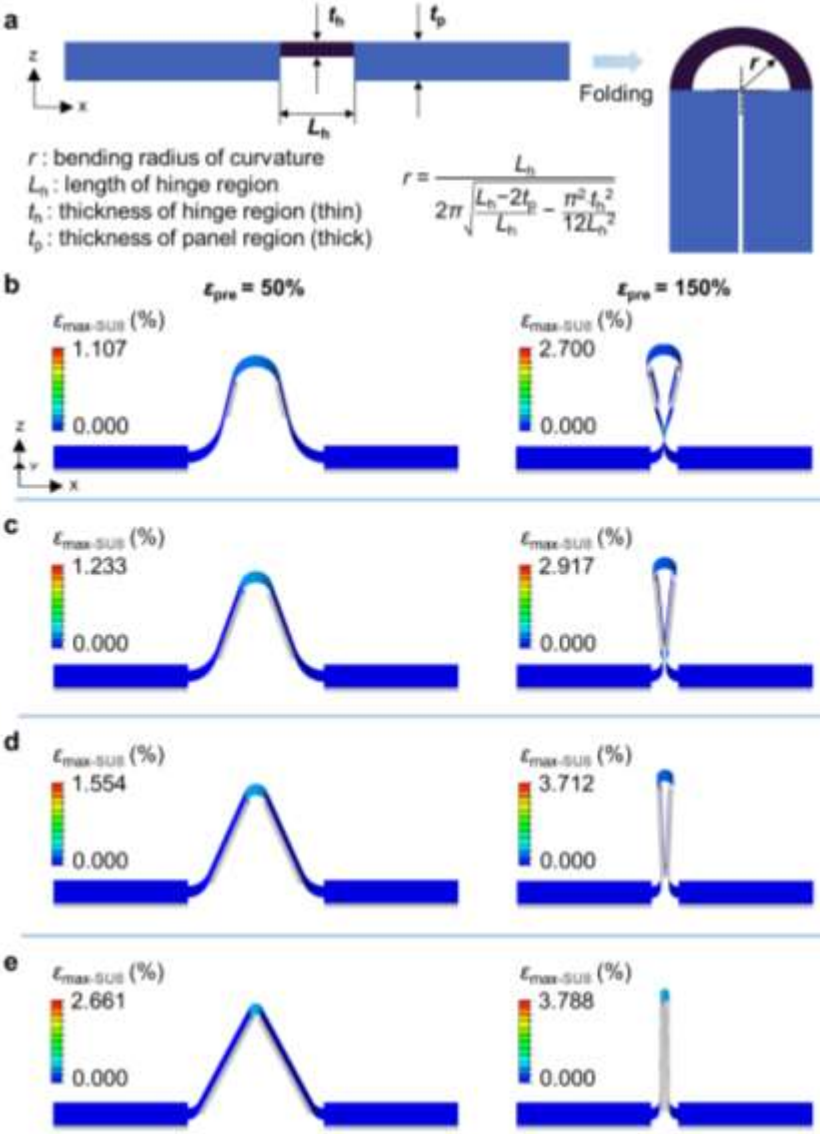

Figure S3. FEA results for the maximum principal strain distributions in the SU8 layer with variations in the length ratio (L_h/L_n). Four different length ratios of b) 0.25, c) 0.15, d) 0.1, e) 0.05. The calculated radius of curvature (r) of 3.43, 2.18, 1.57, 1.16 μm respectively using the theoretical equation a)[1] in the given condition of thickness (t_h = 0.1 and t_p = 1.4 μm).

[1] S.-I. Park, J.-H. Ahn, X. Feng, S. Wang, Y. Huang, J. A. Rogers, *Adv. Func. Mater.* **2008**, *18*, 2673.

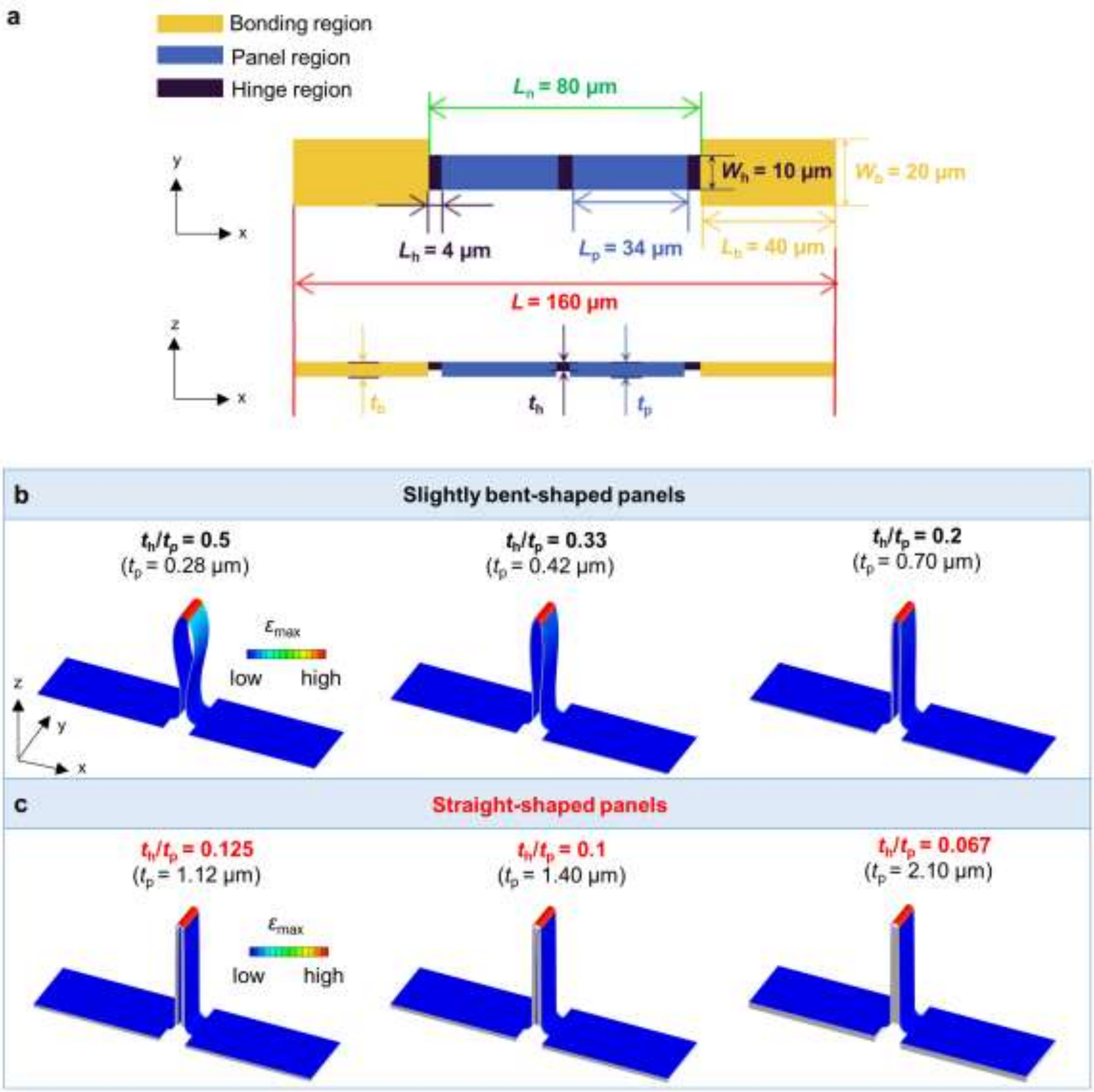

Figure S4. Threshold of thickness ratio (t_h/t_p) in the formation of sharp folding structures, with given length parameters. a) Top view of a 2D precursor with optimized length parameters at selected regions. Cross-sectional view of a 2D precursor with engineered thickness allocations in different regions. b)-c) FEA predictions of deformed shapes of single foldable structures controlled by thickness ratio (with fixed SU8 thickness of t_h = 140 nm, under 150% pretrain). To realize a sharp folding structure, the thick regions (i.e., panel and bonding regions) should be straight-shaped and unbent as a result of sufficient thickness ($t_p >$ ~1.1 μm) to offer high stiffness during 3D assembly.

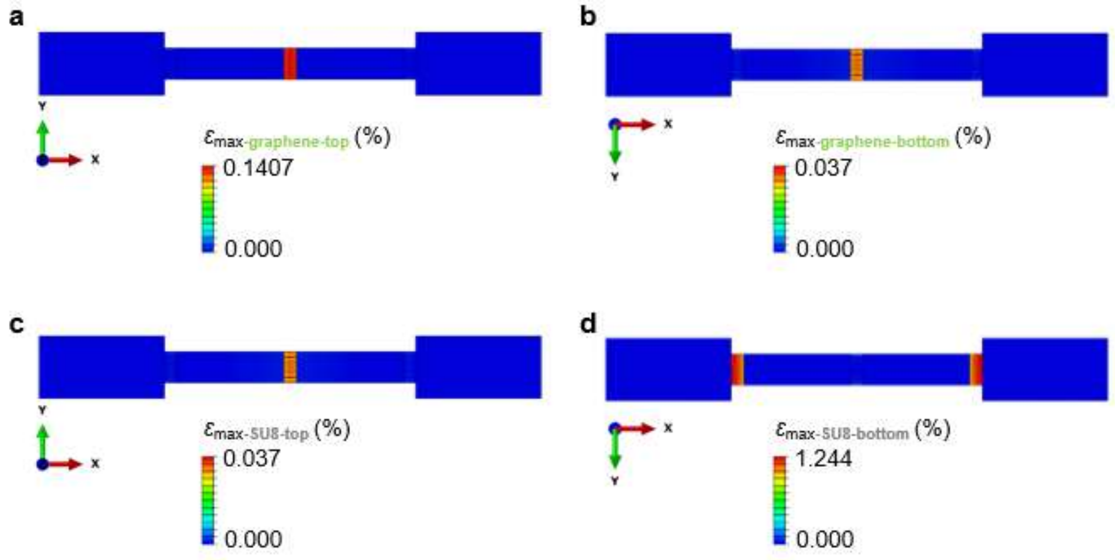

Figure S5. Strain distributions on graphene and SU8 layers (top and bottom surfaces) in a 3D sharp folding microstructure (undeformed configuration) under 180° folding (150% prestrain). The maximum principal strain distributions on the (a) top surface and (b) bottom surface of the graphene layer and the (c) top surface and (d) bottom surface of the SU8 layer, respectively. The hinge section in this figure consists of graphene (1.34 nm)/SU8 (30 nm) and the length of all three hinges L_h is 4 μm.

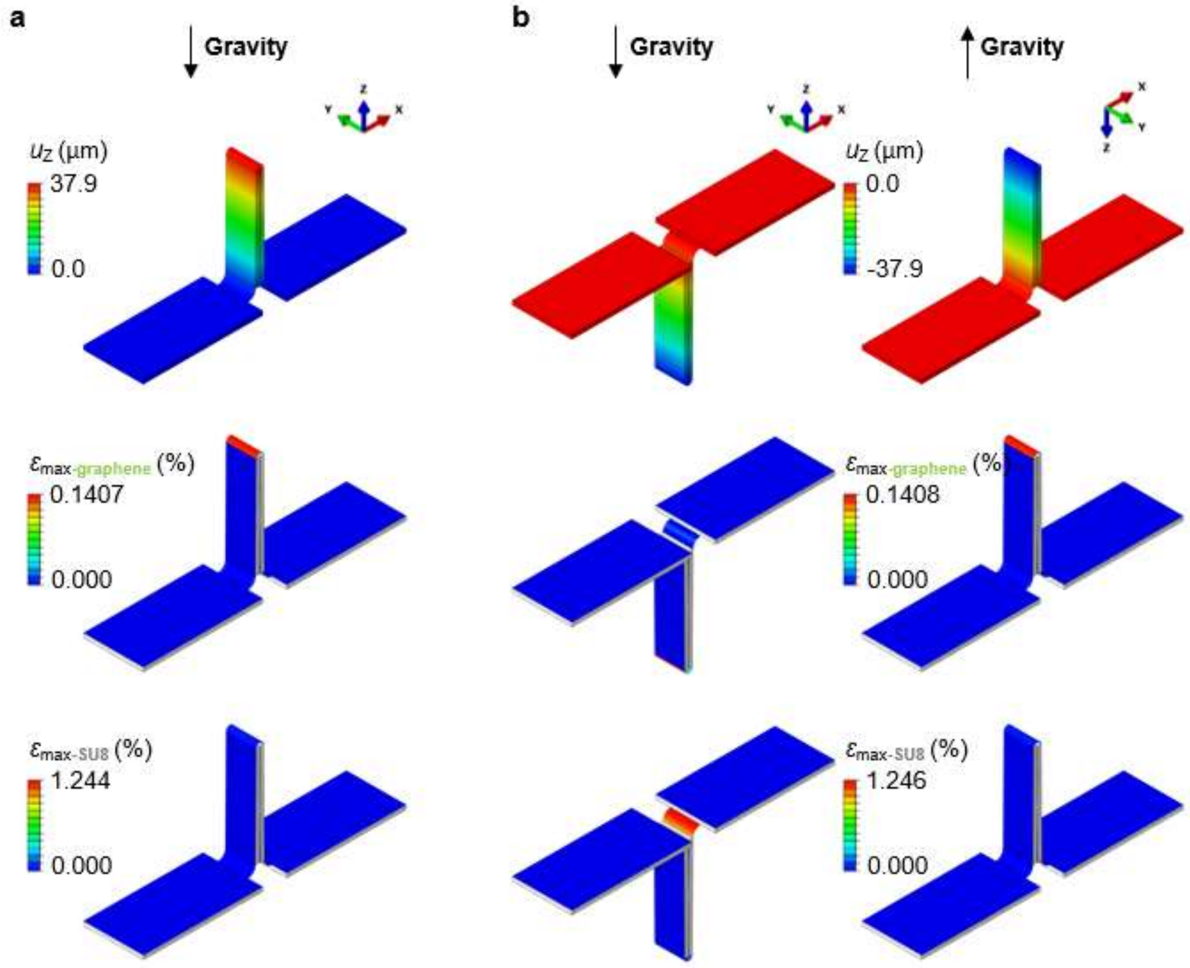

Figure S6. FEA study shows the effect of gravity is negligible on the deformed shape and associated strain distribution of 3D sharp folding microstructures. The contour of out-of-plane displacement u_Z and the maximum principal strain distributions on graphene and SU8 layers for a 3D microstructure facing up (a) or down (b) under gravity. The hinge section in this figure consists of graphene (1.34 nm)/SU8 (30 nm) and the length of all three hinges L_h is 4 μm.

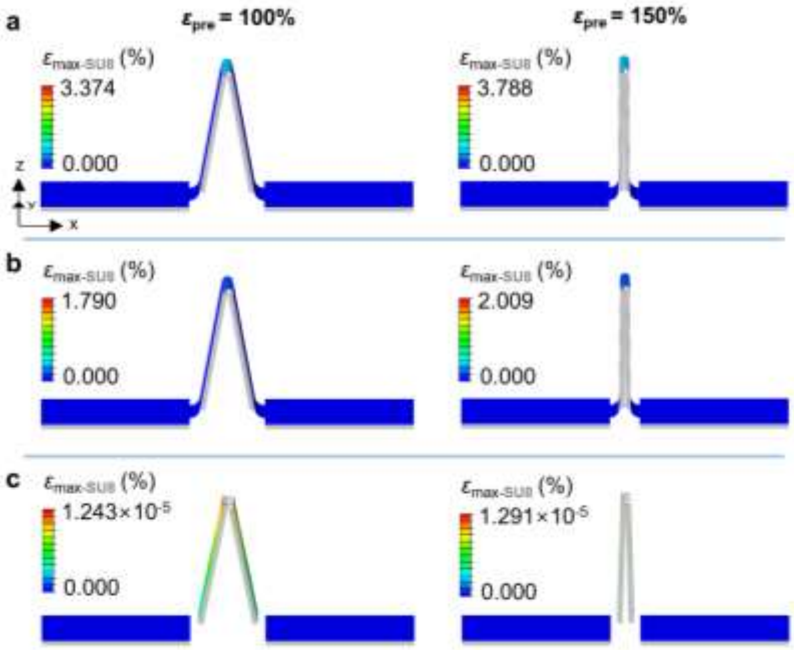

Figure S7. FEA results for the maximum principal strain distribution in the SU8 layer according to three different designs of hinge region. Three different thicknesses of hinge regions include graphene (1.34 nm)/SU8 (100 nm) hinge type a) graphene (1.34 nm)/ SU8 (50 nm) hinge type b) and graphene (1.34 nm) hinge type c).

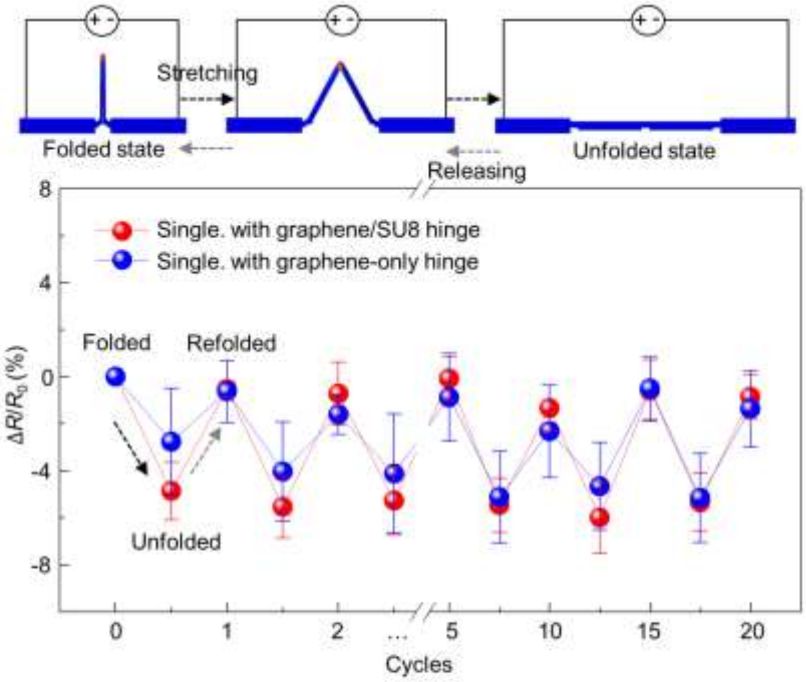

Figure S8. Measurement results for the relative resistance change for the single-folded structures during repeated, cyclic folding and unfolding processes. Black and gray colors denote the stretching and releasing operation, respectively, under 150% prestrain.

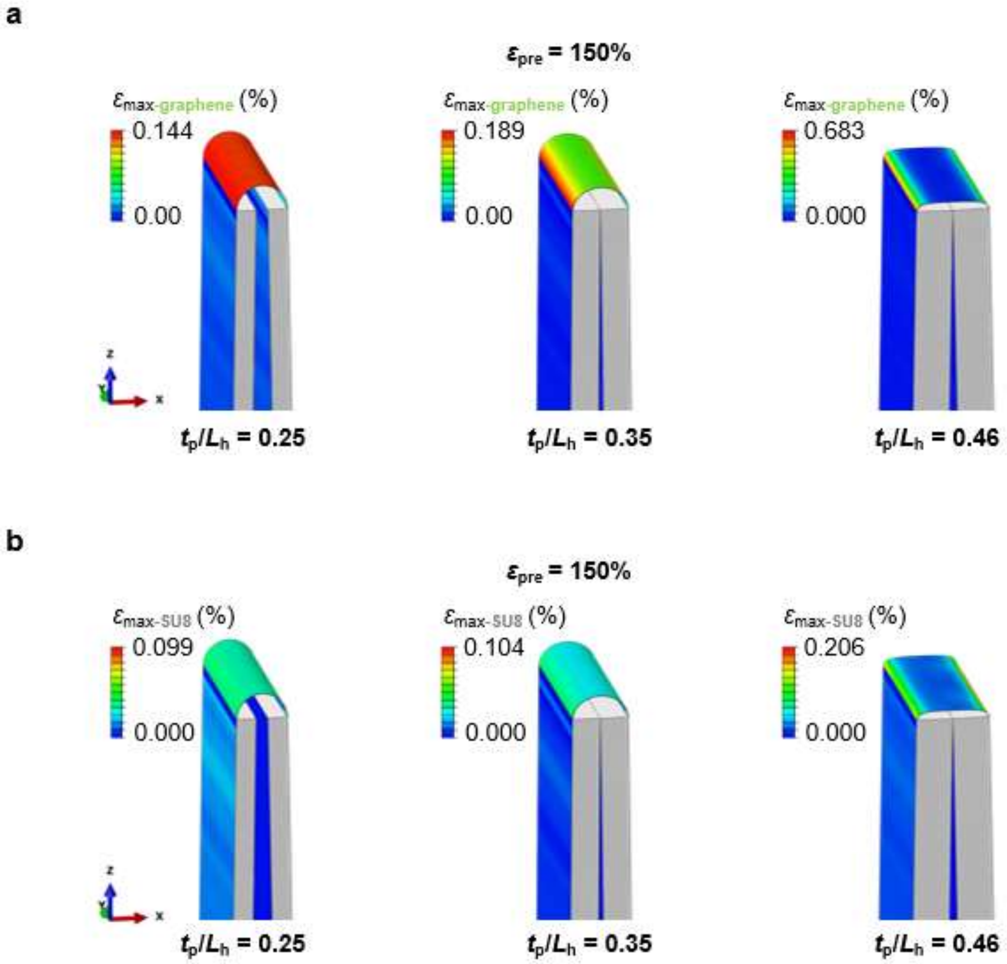

Figure S9. FEA studies of the effects of t_p/L_h (thickness of panel/length of hinge) on the deformed shape and associated strain distribution of the top hinge. The maximum principal strain distributions on (a) graphene layer and (b) SU8 layer in the deformed configuration. The hinge section in this figure consists of graphene (1.34 nm)/SU8 (30 nm) and the length of the hinge L_h is 4 µm. With a value t_p/L_h approaching 0.5, the hinge deforms into a flatter shape and induces higher a material strain.

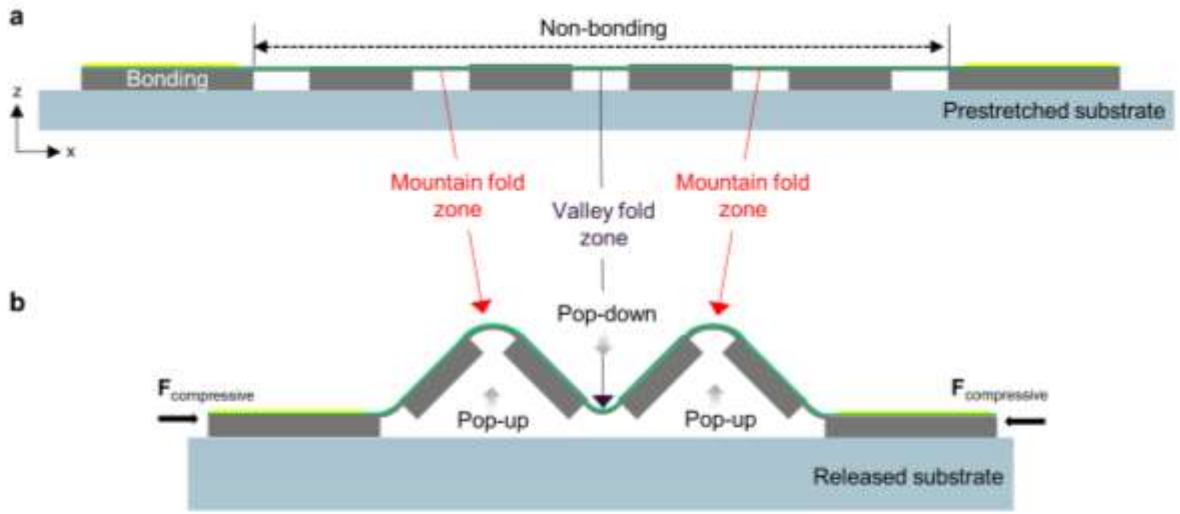

Figure S10. Folding mechanism for multiple-peak foldable structures with two different folding motions including ‘popping-up’ at mountain fold zones and ‘popping-down’ at valley fold zones. a) Initial state of a patterned 2D precursor on a pre-stretched elastomer. b) Folding behavior of the 3D structure driven by releasing the prestrain in the elastomer substrate.

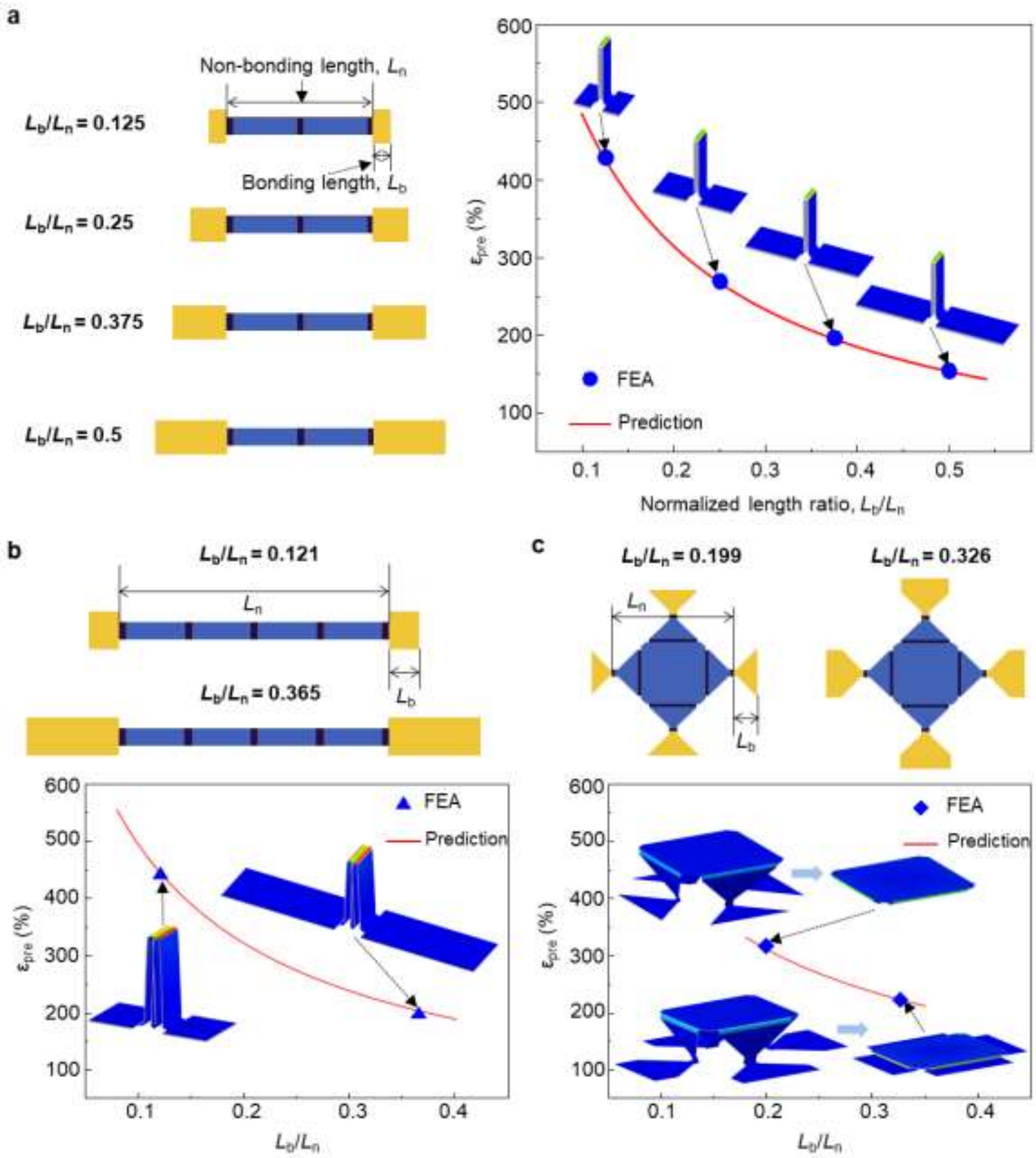

Figure S11. Variation in the required prestrain levels in the formation of sharp folding structures by engineering the size of bonding pads (yellow color). a) Illustration of 2D precursors with four different sizes of the bonding pads by showing the normalized length ratio (L_b/L_n). Corresponding FEA results denote that the required prestrain gradually decreases (from 429% to 155%), as the size of bonding pad increases (with given thickness parameters). b)-c) Effect of a larger size of bonding pads on the required levels of prestrain to realize the multiple-peak and table-shaped foldable structures.

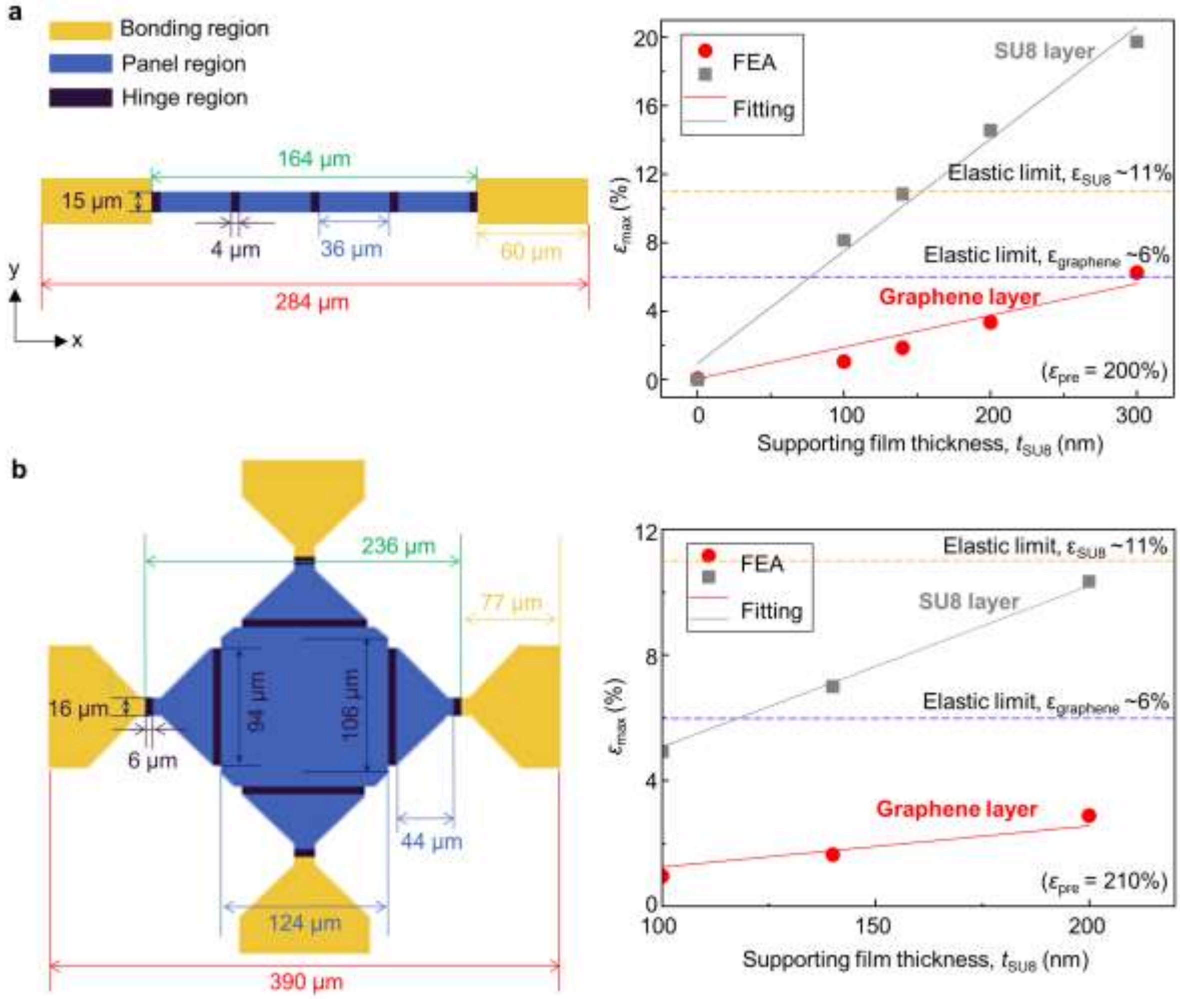

Figure S12. Optimized design of 2D precursors and film thickness control of hinge section for elastic deformation of complex microstructures. a)-b) Schematic diagram for optimized length parameters of selected regions associated with 2D precursors for a) multiple foldable structure and b) table-shaped foldable structure, and FEA results of maximum principal strain depending on the thickness of supporting film in hinge regions (the thick regions include given SU8 thickness of 1.4 µm).

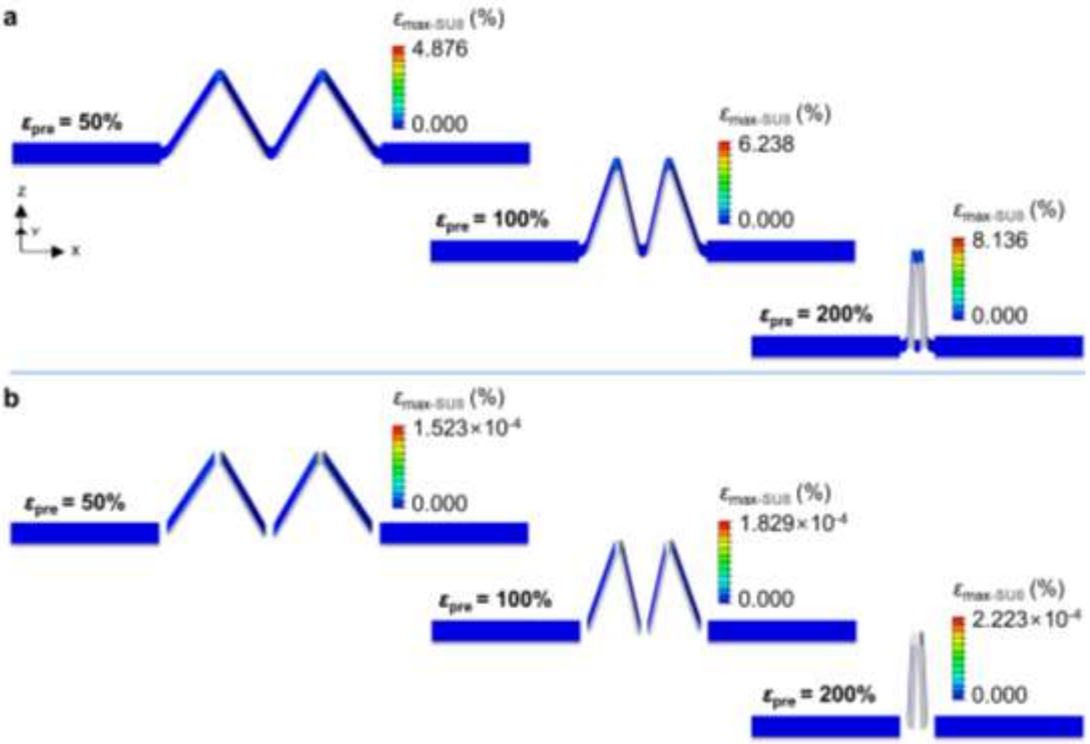

Figure S13. FEA results for the maximum principal strain distribution on SU8 layer with two different designs of hinge region. Two different thicknesses of hinge regions of multiple-peak foldable structures in Figure 3. Graphene/SU8 (1.34/100 nm) hinge type a) and graphene (1.34 nm) hinge type b).

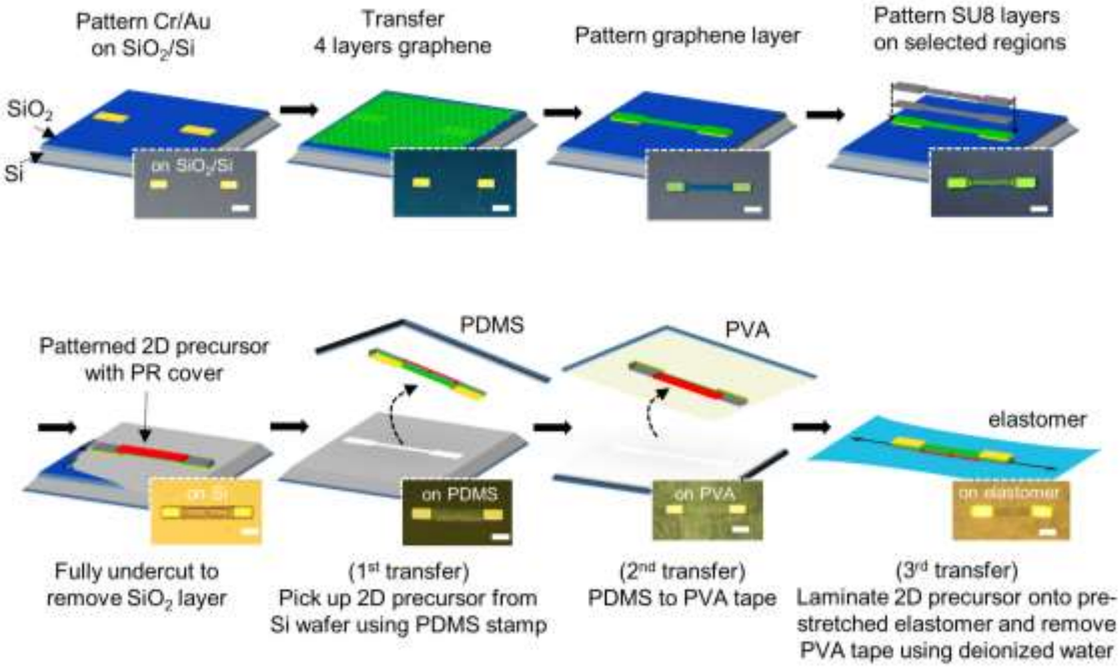

Figure S14. Schematic diagram and optical images for the fabrication processes in the controlled buckling-driven 3D formation of origami microstructures based on graphene (scale bar, 40 µm).

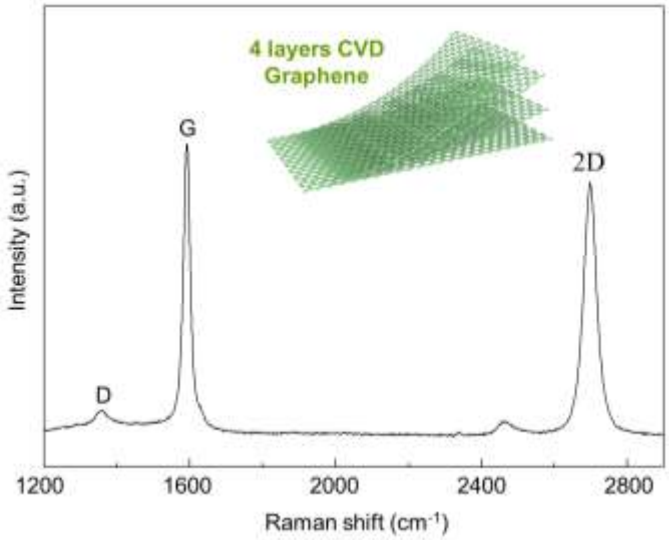

Figure S15. Optical characterization of 4 layers CVD graphene on SiO_2/Si wafer. Raman spectra of graphene film (G peak at 1591 cm^{-1} and 2D peak at 2697 cm^{-1}).